Journal of Materials Chemistry C

ROYAL SOCIETY OF CHEMISTRY

PAPER

View Article Online
View Journal | View Issue

Cite this: J. Mater. Chem. C, 2025, 13, 20602

Growth of $MnWO_4$ nanowires on W(110) by high-temperature oxygen-assisted molecular beam epitaxy

Kalina Fornal,[a] Clara Gutiérrez-Cuesta,[b] Adolfo del Campo,[c] Anna Mandziak,[d] Pawel Nita,[de] José Emilio Prieto,[b] José F. Marco[b] and Juan de la Figuera *[b]

We describe the growth of synthetic hübnerite ($MnWO_4$) by high-temperature oxygen-assisted molecular beam epitaxy on W(110). The hübnerite nanowires have widths of hundreds of nanometers, heights of tens of nanometers and lengths in the range of millimeters. The growth was followed in real time by low-energy electron microscopy (LEEM). The nanowires were characterized *in situ* by low-energy electron microscopy, X-ray absorption and X-ray photoelectron spectroscopy in photoemission microscopy, as well as *ex situ* by atomic force microscopy, optical microscopy and Raman spectroscopy. Hübnerite can be grown on W(110) by dosing only manganese in a molecular oxygen environment, likely due to the formation of highly mobile WO_x species with diffusion lengths of the order of hundreds of micrometers. These species can react with the deposited Mn and be efficiently incorporated into the wolframite structure of hübnerite. The strongly anisotropic growth observed may stem from the inherent anisotropy of the wolframite lattice. We propose that this method may be applicable to the growth of other tungstates as well.

Received 11th July 2025,
Accepted 2nd September 2025

DOI: 10.1039/d5tc02639c

rsc.li/materials-c

1 Introduction

Synthetic hübnerite, $MnWO_4$, has been suggested as a multifunctional material[1] in fields such as photocatalysis,[2–4] or for applications in supercapacitors.[5] It is insulating with a band gap higher than 2.6 eV, and thus transparent to visible light. Below 13 K it is a single phase multiferroic material[6–9] combining a spiral magnetic ordering with ferroelectricity.

Hübnerite belongs to the family of the tungstates of the 3d transition metals such as $FeWO_4$, $CoWO_4$ or $NiWO_4$, which all share the same wolframite structure. Wolframite, the iron–manganese tungstate, is itself one of the most common commercial tungsten ores.[10] The wolframite structure belongs to the monoclinic $P2/c$ space group. It is composed of edge-sharing oxygen distorted octahedra surrounding W^{6+} and Mn^{2+} cations, forming zig-zag chains.

Nanowires are of interest from an applied point of view, often presenting a high surface-to-volume ratio. From a fundamental perspective they are useful for studying confinement in the perpendicular directions while keeping bulk-like properties in the axial direction. They possess morphologies which can benefit from the application of novel growth methods.[11–13] In the particular case of hübnerite nanowires, their growth has been performed by the solvothermal method,[14] and by incorporation of Mn onto $W_{18}O_{49}$ nanowires.[15] Instead, in the present work, we describe the growth of hübnerite nanowires on W(110) single crystals by oxygen-assisted high-temperature molecular beam epitaxy (MBE) depositing only the manganese component and taking advantage of the special characteristics of the oxygen-tungsten interaction to provide the tungsten component.

The growth of oxide ultrathin films and nanostructures on metal substrates has advantages for their characterization, as well as interest for applications in catalysis.[16] Our method consists of depositing the required cations from a metallic source in a background of oxidizing gas like molecular oxygen at a temperature high enough to activate surface diffusion, coupled to real time observations by low-energy electron microscopy (LEEM).[17] One prerequisite for such approach to be successful is that the substrate is less easily oxidized than the deposited metal. Using this procedure, we have grown spinel and rock-salt oxides on Ru(0001) single crystals as well as on Ru(0001) thin films on sapphire. Complication factors are that often three-dimensional growth is achieved and that different

[a] University of Aberdeen, Aberdeen, UK
[b] Instituto de Química Física Blas Cabrera, CSIC, Madrid 28006, Spain. E-mail: juan.delafiguera@csic.es
[c] Instituto de Cerámica y Vidrio, CSIC, Madrid 28049, Spain
[d] Solaris National Synchrotron Radiation Centre, Kraków 30-392, Poland
[e] Faculty of Physics, Astronomy and Applied Computer Science, Jagiellonian University, Kraków 30-348, Poland

oxide phases might be present on the surface. Even taking into account these problems, high-temperature oxygen-assisted MBE growth allows obtaining, for example, ferrimagnetic micrometer-wide crystals of iron-containing oxides such as magnetite,[18] maghemite,[19] cobalt ferrite[20] and nickel ferrite,[21] with magnetic domains which are orders of magnitude larger than those usually found in typical thin films. Cobalt[22] and nickel oxide[23] antiferromagnetic crystals have also been grown in this way, as well as ceria.[24] In all those cases, ruthenium acts as an inert substrate which plays only a minor role in the growth process by breaking oxygen molecules into atomic oxygen and providing an epitaxial template with a Ru–Ru distance which is close to the oxygen–oxygen distance in the oxides.

However, when attempting the same approach to grow oxides on W(110), the role of the substrate is very different. This is related to the different oxide formation mechanism and reactivity of ruthenium and tungsten. For low oxygen exposures, both the Ru(0001)[25,26] and W(110)[27] surfaces are covered by an atomic layer of oxygen chemisorbed on the surface, which upon cooling to room temperature gives rise to coverage-dependent ordered structures. Increasing the oxygen dose results in the formation of genuine oxide crystals. In the case of Ru(0001), the growth takes place initially in the form of RuO_2 islands having the rutile structure. A higher oxygen pressure or a stronger oxydizing agent such as NO_2[28–30] is required to further grow the oxide islands on this substrate. But RuO_2 is very stable in UHV.[29] Tungsten, instead, gives rise to WO_3 upon oxidizing.[31] Many studies determined that WO_3 has a much higher vapour pressure than RuO_2, and that it sublimates into several tungsten oxides in UHV conditions at temperatures around 1400 K[32–34] explaining the propensity of tungsten to be etched by oxygen, as initially studied by Langmuir.[35,36] Even before sublimation, it is likely that WO_x units are highly mobile on the W surface, presumably by a ''sky-hook'' effect in which an adsorbate enhances surface diffusion by weakening the bonding of the adatoms to the substrate as observed in S/Cu(111)[37,38] and other systems.[39,40] These oxide units would provide a source of W^{6+} for the growth of ternary oxides upon deposition of an additional cation. This effect has been observed in the growth of cerium tungstate during the initial stages of the deposition of cerium on W(110) in a molecular oxygen background pressure[41,42] at 700 K. With continued deposition, a pure cerium oxide was obtained, as the transport of W^{6+} through the tungstate is kinetically hindered. If however, the growth mode is purely three dimensional, the availability of W^{6+} is still possible through the uncovered areas.

2 Experimental

The growth was performed at the low-energy electron-microscopy (LEEM) facility of the Instituto de Química Física Blas Cabrera in Madrid and at the DEMETER beamline of the Solaris synchrotron in Kraków. Both sites are equipped with Elmitec LEEM III instruments; in the latter case, it is integrated with a hemispherical energy spectrometer. Using an electron beam as the illumination source, both microscopes can acquire LEEM images of the surface during growth by MBE, as well as low-energy electron diffraction patterns. At Solaris, the DEMETER-PEEM instrument uses a soft X-ray beam to illuminate the sample, causing it to emit electrons through X-ray absorption and photoemission. These emitted electrons are used to create images that reveal the chemical composition of the sample. By tuning the energy of the X-ray beam, the instrument can produce spatially resolved X-ray absorption spectra. Additionally, the built-in energy spectrometer allows to perform X-ray photoelectron spectroscopy (XPS) from specific regions of the sample.

The W(110) crystal used as a substrate was cleaned by multiple steps of flashing at 1500 °C in a molecular oxygen atmosphere (1×10^{-6} mbar). Manganese was deposited from a 5 mm thick manganese rod inside a home-made electron bombardment doser. The dose rate was calibrated by depositing manganese on the clean W(110) surface. *Ex situ* characterization of the nanostructures was performed by optical microscopy, atomic force microscopy and Raman spectroscopy. The Raman spectra were acquired with a commercial Witec Alpha 300RA confocal Raman spectrometer, using a 100× objective with a numerical aperture of 0.95. The light source was a 532 nm laser operated at 1 mW power, selected in order to avoid modification of the samples. The spectra presented are the average of 5 scans, each acquired with a 30 s integration time.

3 Results and discussion

In order to grow an oxide by oxygen-assisted MBE, crucial parameters are the oxygen pressure and the substrate temperature. As discussed in detail in ref. 43, a pressure of 10^{-6} mbar, compatible with direct observation by LEEM, should be able to oxidize Mn to Mn^{2+} at any growth temperature. The growth temperature of 800 °C was selected based on the previous experience with the growth by oxygen-assisted MBE of rock-salt and spinel oxides on Ru(0001).[18,20,22] On the one hand, the temperature should be as high as possible to promote long-range diffusion of the deposited species and to promote good crystallinity. On the other hand, the temperature should be low enough so that the desired oxide does not decompose. Given that W-oxides decompose at temperatures above 1000 °C, we selected 800 °C in this work. We have later confirmed that the nanostructures grown decompose at a temperature of 850 °C.

A sequence of images from a movie acquired during the deposition of manganese on the oxygen-coveredW(110) surface at 800 °C is shown in Fig. 1. The starting surface, which presents atomic steps imaged as faint dark lines in the first frame (Fig. 1a), was already exposed for several minutes to a pressure of 1×10^{-6} mbar of molecular oxygen. With these conditions, if the sample is cooled down to room temperature, it presents the so-called 337 reconstruction.[44,45] From etching experiments of oxygen on tungsten[31,34] it is clear that at elevated temperatures, it involves mobile WO_x units. The manganese

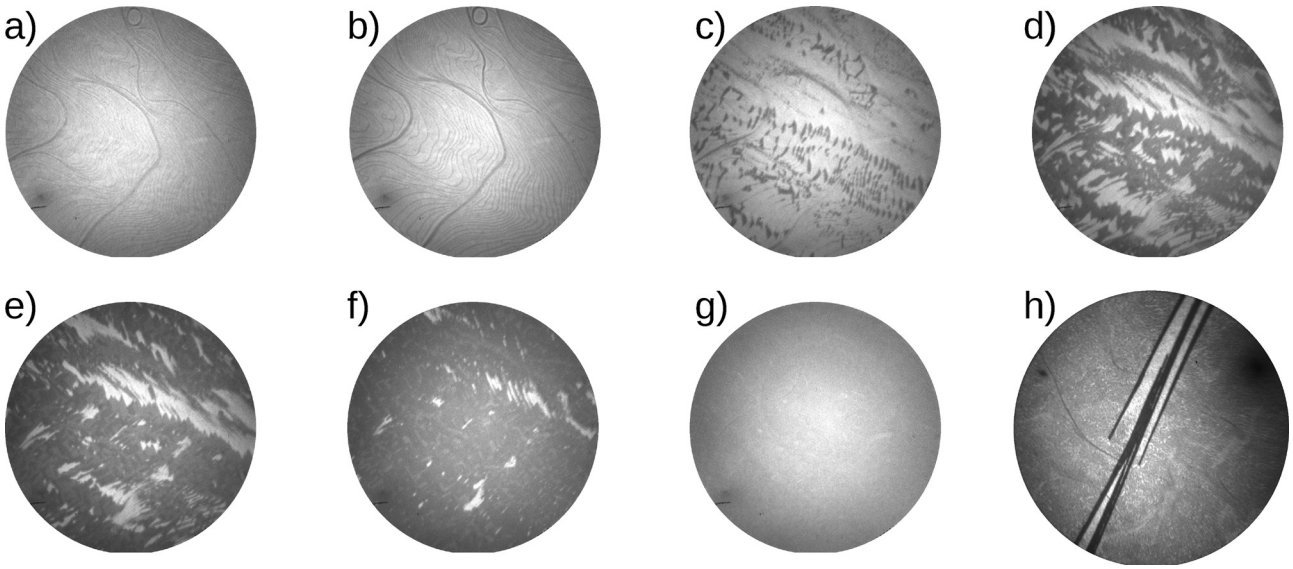

Fig. 1 Sequence of LEEM images (a)–(g) showing the initial growth of manganese on W(110) under oxygen exposure (1×10^{-6} mbar) at 800 °C, and the nanowire formed after postannealing at 800 °C (h). Image g, which shows the closure of the first layer, was taken after 17.5 min of growth. The field of view is 15 μm.

doser shutter was opened just before the acquisition of Fig. 1b, where islands initially nucleate at the steps, and then grow into larger sizes (Fig. 1c–e). The initial surface is nearly completely covered in Fig. 1f. In Fig. 1g the complete surface is already covered by a mixed Mn–W oxide. Continuing the deposition, eventually some nanostructures were detected on the surface; their growth could be followed in LEEM. However, the nucleation rate is very small, with just a few structures found in millimeter-sized areas. The sample was then cooled down in oxygen for further characterization. The grown structures decompose at a temperature of 850 °C.

An alternative way of obtaining the nanostructures, still with a very low density, was to stop the growth after the surface is completely covered by a mixed Mn–W layer and to cool down to room temperature. The sample was then transferred (in air) from the Madrid LEEM instrument into the Solaris one for further processing and characterization. In the Solaris station, the sample was initially degassed for several hours at 250 °C. At such stage, the surface still looked the same in LEEM as observed in the Madrid instrument. After a brief anneal to 800 °C in vacuum for a few minutes, again a few nanostructures could be located on the surface of the crystal. Fig. 1h shows a low-energy electron microscopy (LEEM) image of the central region of a nanostructure with a distinctly elongated shape. This structure is composed of several nanowires that appear to branch out from a common central point, where a zig-zag pattern is visible. The same region is shown in photoemission microscopy (Fig. 2a) and with a wider field of view in Fig. 2b using *ex situ* optical microscopy, revealing that the nanowires extend to lengths of several hundred micrometers. Fig. 2c presents an atomic force microscopy (AFM) image of the same area, acquired in contact mode. As illustrated by the height profile in Fig. 2d, the nanowires range in width from several hundred nanometers to nearly one micrometer, with heights

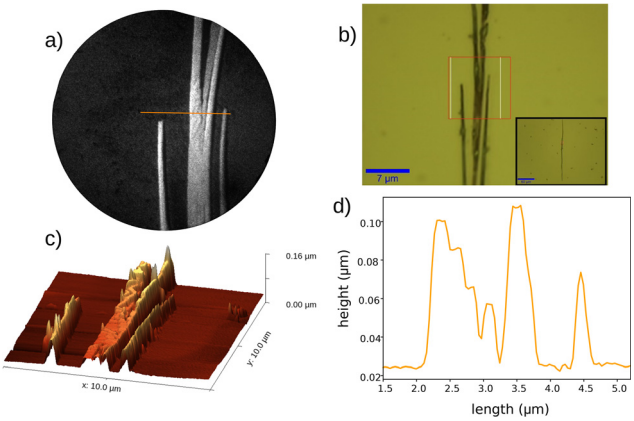

Fig. 2 Correlative microscopy on the $MnWO_4$ nanowire. (a) PEEM microscopy (at the Mn L_3 edge maximum) with a field of view of 15 μm. (b) Optical microscopy of the same general area at two different magnifications. (c) Atomic force microscopy (AFM) of the same region as in a). (d) Height profile along the line marked in the PEEM image (the data comes from the AFM image).

reaching up to 100 nanometers. The zig-zag feature is clearly resolved in the AFM image and is seen to increase in height along its length.

In order to determine the composition and structure of the nanowires, we resorted to the use of several selected-area spectroscopies. We first present in Fig. 3 the X-ray absorption spectra at the Mn $L_{2,3}$ edges and at the O K-edge. In the first case, the two main structures appear well separated, by about 10 eV, due to the spin–orbit splitting between the $2p_{\frac{1}{2}}$ and $2p_{\frac{3}{2}}$ core levels. The L_3 structure appears in the range 637–645 eV, while the L_2 appears in the 650–655 eV range. The manganese spectrum has been reported for both manganese oxide and

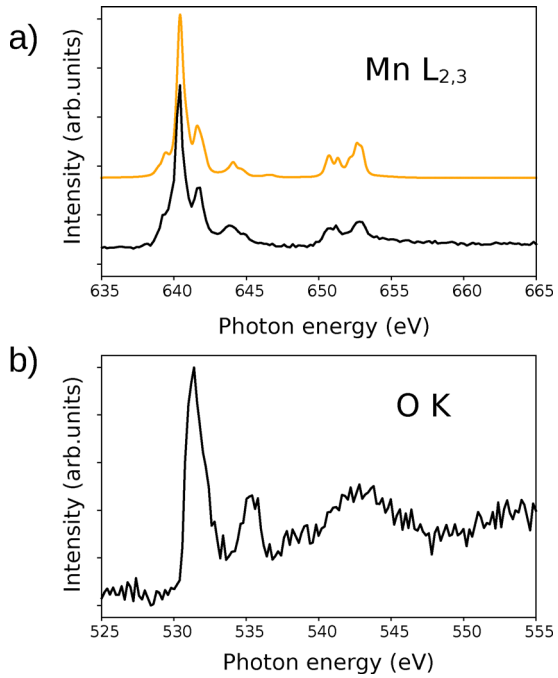

Fig. 3 XAS spectrum (black) acquired from the central part of the wire shown in Fig. 2a. (a) XAS spectra at the Mn L_2 and L_3 absorption edges. Shifted up, in orange, a multiplet calculation is shown (details in the main text). (b) XAS spectrum at the oxygen K-edge.

manganese tungstate.[46] The shape of each absorption edge, specially in the case of the L_3 one, depends strongly on the multiplet structure, the effects of the local crystal fields and hybridization with the O 2p ligands and on the Mn 3d–3d and 2p–3d Coulomb and exchange interactions. We note that the Mn XAS signal from the areas outside the nanowires presented roughly the same shape (not shown) although the signal was quite noisy with very low intensity. For the oxygen edge, the signal outside the nanowires was negative, indicating that it was dominated by the absorption by oxygen in the mirrors of the X-ray optics prior to the PEEM instrument. We used it to normalize the spectra from the nanowire, shown in Fig. 3b.

To model the Mn experimental spectra, we calculated the X-ray absorption spectra using the Quanty[47] code *via* the Crispy interface.[48] The spectrum (Fig. 3a, shown in orange) has been calculated for octahedrally coordinated Mn^{2+} ions. We have used a 10*Dq* crystal field of 0.9 eV (as reported by variable pressure studies on $MnWO_4$[49]) and a spin–orbit coupling of 7.0 eV was chosen to best fit the experimental data. The values for intra-atomic 3d–3d and 2p–3d Coulomb interactions were taken from ref. 46 as 7.0 eV and 8.0 eV, respectively and the Slater integrals were reduced to 83% of their Hartree–Fock values. The simulated spectrum reproduces well the experimental peak positions and general shapes of the absorption edges, indicating the presence of high-spin, octahedrally coordinated Mn^{2+} ions in the structure.

For the O K-edge, the multiplet effects and the core-hole spin–orbit coupling do not need to be taken into account, since the core-hole resides in a spherically symmetrical 1s orbital localized on the oxygen atom. In fact, the shape of the O K-edge spectra shows a more direct correspondence with the empty p-states on the oxygen as they are affected by hybridization with the metal cations.[50,51] The O K-edge X-ray absorption spectrum (Fig. 3b) can be divided into three regions. The first one consists of the intense peak at 532 eV. The second comprises the peak at 536 eV and the third the broader feature at 540–548 eV. The first region corresponds to electronic transitions to the unoccupied oxygen 2p states[50,52] hybridized with the empty W^{6+} t_{2g} orbitals, with some minor additional contribution from the manganese d levels (which are just less than 1 eV apart). The second peak is likely associated to hybridized oxygen 2p orbitals with the W^{6+} e_g levels, which are located approximately 5 eV above the t_{2g} levels in WO_3.[52] This interpretation is supported by the fact that WO_3, like $MnWO_4$, exhibits octahedral coordination around the tungsten atoms. In our case, the separation between them, which is directly the crystal field 10*Dq* parameter, would then be 4.0 eV. Finally, the third broader feature is attributed to the hybridization of oxygen states with the more delocalized s and p orbitals of the cations conduction band.[52]

Spatially resolved W 4f X-ray photoelectron spectra were acquired from the wire and the surrounding area with a photon energy of 200 eV; they are shown in Fig. 4. The W 4f spectral region is quite complex showing three different spin–orbit doublets which suggests that tungsten is present in three different chemical states at the surface both at the nanowire and the outside region. The peaks near 33.5 eV and 31.3 eV can be assigned to metallic tungsten, while those at about 38.5 eV and 36.4 eV correspond to a W^{6+} chemical species.[53] W^{6+} peaks

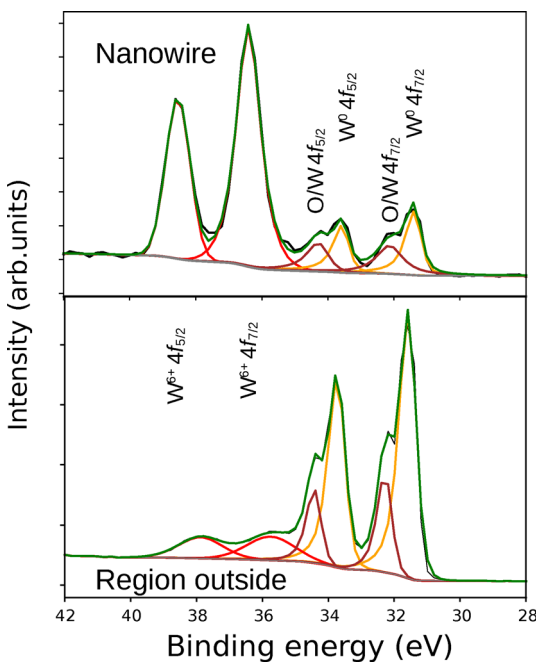

Fig. 4 W 4f XPS spectra acquired from the $MnWO_4$ nanowire and from the outside region (black: experimental data, gray: Shirley background). The fit is discussed in the text.

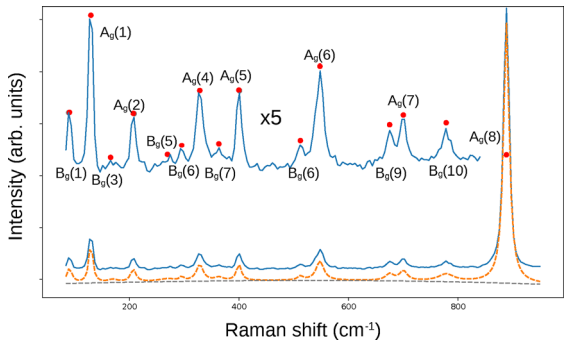

Fig. 5 Raman spectra acquired from the $MnWO_4$ nanowire. Experimental data are shown in blue with the inset showing an expanded scale with the reported modes marked by red dots). A fit (described in the text) as well as the identification of the various peaks observed is included.

are expected to appear at energies about 6 eV higher than those corresponding to metallic tungsten due to the increased charge on the ions. The difference observed in our spectra amounts to 5 eV in the case of the wire, and to 4.2 eV in the case of wetting layer, where the W^{6+} are shifted to slighly lower binding energies (by 0.5–0.7 eV with respect to the wire). As it has been noted in the discussion of the XAS spectra, the ligand–metal charge transfer between oxygen and tungsten lowers the formal charge of the tungsten cation, resulting in a smaller energy difference between peaks. In any case, the chemical shifts noted in our spectra remain in agreement with values published for W^{6+} compounds. Finally, the doublet appearing at binding energies slightly higher than those of the doublet corresponding to metallic tungsten has been associated with the occurrence of regions in the sample where oxygen is adsorbed on metallic tungsten. This brings about a slight decrease in electron density on tungsten and, hence, a small increase in the corresponding binding energies of the W 4f core levels. The main difference between both regions is the relative weight of the different components: while the nanowire is composed mostly of W^{6+}, the metallic W and O/W components dominate in the outside region.

Fig. 5 shows a characteristic Raman spectrum acquired from the central part of the wire (no Raman peaks were detected outside the nanowires). The wolframite monoclinic structure has a large number (36) of phonon modes as obtained from group-theory analysis ($8A_g + 10B_g + 8A_u + 10B_u$).[54] Of those, there should be 18 Raman-active modes ($8A_g + 10B_g$). While there are studies performed on hübnerite minerals,[55–58] a more complete characterization has been performed by polarized Raman on single crystals of $MnWO_4$,[59] detecting all the Raman active phonon modes and identifying their atomic vibrations by means of density functional calculations. In our case, we readily detect (Fig. 5) nearly all the 18 modes in our nanowire (marked in the inset by red dots). The remaining modes, $B_g(2,4)$ and $A_g(3)$ have intensities close to the noise level. We have fitted the spectrum to a sum of Lorentzian peaks and a third-order polynomial for the background (shown by an orange dashed line). The fitted Lorentzian peak positions, widths and amplitudes are shown in Table 1, together with the values reported

Table 1 Raman modes detected in the nanowires, compared with the reference work in ref. 59

Mode	Ref. 59 cm^{-1}	Position cm^{-1}	Width cm^{-1}	Amplitude arb. units
$B_g(1)$	89	90	6	56
$A_g(1)$	129	129	4	158
$B_g(2)$	160	—	—	—
$B_g(3)$	166	170	10	10
$B_g(4)$	177	—	—	—
$A_g(2)$	206	207	6	48
$A_g(3)$	258	—	—	
$B_g(5)$	272	269	20	10
$B_g(6)$	294	295	3	16
$A_g(4)$	327	328	8	62
$B_g(7)$	356	363	9	13
$A_g(5)$	397	400	5	62
$B_g(8)$	512	512	6	15
$A_g(6)$	545	548	8	72
$B_g(9)$	674	675	9	25
$A_g(7)$	698	700	8	37
$B_g(10)$	774	778	17	27
$A_g(8)$	885	888	6	1000

for a single crystal.[59] The difference between the single-crystal results and the nanowire grown on W(110) is at most 3 cm^{-1}, suggesting that our $MnWO_4$ is also a single crystal. Thus the nanowire is thick enough to relax to the bulk structure of hübnerite. A promising venue to research is to study ultrathin wires to find possible structural modifications or phonon confinement effects for nanostructures like those obtained before the last annealing stage.

4 Conclusions

We have grown nanostructured synthetic hübnerite ($MnWO_4$) by molecular beam epitaxy of manganese on a W(110) substrate in a molecular oxygen background. The nanostructures have been characterized by both *in situ* (X-ray absorption and X-ray photoelectron spectroscopies as well as low-energy electron microscopy) and *ex situ* (Raman spectroscopy and atomic force microscopy) techniques. The formation of a highly diffusive tungsten oxide allows for the growth of the tungstate by depositing only manganese. The nanostructures are tens of nanometers thick, hundreds of nanometers wide and with lengths in the range of millimetres. From current experiments which we will submit shortly to the scientific literature, we propose that this simple growth method based on the deposition of a single metal on W(110) by high-temperature oxygen-assisted molecular beam epitaxy can be successfully extended to the growth of other transition metal or alkaline-earth tungstates, although the particular morphology of the grown nanostructures will likely depend on whether more isotropic (*e.g.* tetragonal scheelite) or more anisotropic (*e.g.* monoclinic wolframite) structures are formed.

Author contributions

The work was planned by JdlF and JEP, the samples were grown by KF and CG-C, and the synchrotron characterization was

performed by AM, PN, CG-C, JdlF. JFM contributed to the XPS analysis and AdC performed the Raman, AFM and optical microscopy. The manuscript was written by JdlF and CG-C with input and revisions from all the other authors.

Conflicts of interest

There are no conflicts to declare.

Data availability

Data are available at the DIGITAL.CSIC open repository under DOI https://doi.org/10.20350/digitalCSIC/17530.

Acknowledgements

This work was supported by Grants PID2021-124585NB-C31 and TED2021-130957B-C54 funded by MCIN/AEI/10.13039/501100011033, by ''ERDF A way of making Europe'' and by the ''European Union NextGenerationEU/PRTR'', and by the BEETHOVEN project funded by the European Commission under grant agreement 101129912. Views and opinions expressed are however those of the author(s) only and do not necessarily reflect those of the European Union or the European Education and Culture Executive Agency (EACEA). Neither the European Union nor EACEA can be held responsible for them. This publication was partially developed under the provision of the Polish Ministry of Science and Higher Education project ''Support for research and development with the use of research infrastructure of the National Synchrotron Radiation Centre Solaris'' under contract no. 1/SOL/2021/2.

References

1 M. Assis, A. C. M. Tello, F. S. A. Abud, P. Negre, L. K. Ribeiro, R. A. P. Ribeiro, S. H. Masunaga, A. E. B. Lima, G. E. Luz Jr, R. F. Jardim, A. B. F. Silva, J. Andrés and E. Longo, *Appl. Surf. Sci.*, 2022, **600**, 154081.
2 X. Li, D. Teschner, V. Streibel, T. Lunkenbein, L. Masliuk, T. Fu, Y. Wang, T. Jones, F. Seitz, F. Girgsdies, F. Rosowski, R. Schlögl and A. Trunschke, *Chem. Sci.*, 2019, **10**, 2429–2443.
3 K. S. Kumar, K. Vaishnavi, P. Venkataswamy, G. Ravi, K. Ramaswamy and M. Vithal, *J. Indian Chem. Soc.*, 2021, **98**, 100140.
4 S. Han, Y. Wang, D. Zhang and H. Cong, *Chem. Commun.*, 2023, **59**, 6857–6860.
5 A. M. Sorouri, A. Sobhani-Nasab, M. R. Ganjali, S. Manani, H. Ehrlich, Y. Joseph and M. Rahimi-Nasrabadi, *Appl. Mater. Today*, 2023, **32**, 101819.
6 O. Heyer, N. Hollmann, I. Klassen, S. Jodlauk, L. Bohaty, P. Becker, J. A. Mydosh, T. Lorenz and D. Khomskii, *J. Phys.: Condens. Matter*, 2006, **18**, L471.
7 A. H. Arkenbout, T. T. M. Palstra, T. Siegrist and T. Kimura, *Phys. Rev. B:Condens. Matter Mater. Phys.*, 2006, **74**, 184431.
8 K. Taniguchi, N. Abe, T. Takenobu, Y. Iwasa and T. Arima, *Phys. Rev. Lett.*, 2006, **97**, 097203.
9 K. Taniguchi, N. Abe, H. Umetsu, H. A. Katori and T. Arima, *Phys. Rev. Lett.*, 2008, **101**, 207205.
10 E. Lassner and W.-D. Schubert, *Tungsten: Properties, Chemistry, Technology of the Element, Alloys, and Chemical Compounds*, Springer, US, Boston, MA, 1999.
11 B. Mandl, J. Stangl, E. Hilner, A. A. Zakharov, K. Hillerich, A. W. Dey, L. Samuelson, G. Bauer, K. Deppert and A. Mikkelsen, *Nano Lett.*, 2010, **10**, 4443–4449.
12 M. Fickenscher, T. Shi, H. E. Jackson, L. M. Smith, J. M. Yarrison-Rice, C. Zheng, P. Miller, J. Etheridge, B. M. Wong, Q. Gao, S. Deshpande, H. H. Tan and C. Jagadish, *Nano Lett.*, 2013, **13**, 1016–1022.
13 K. Pemasiri, H. E. Jackson, L. M. Smith, B. M. Wong, S. Paiman, Q. Gao, H. H. Tan and C. Jagadish, *J. Appl. Phys.*, 2015, **117**, 194306.
14 S.-J. Chen, X.-T. Chen, Z. Xue, J.-H. Zhou, J. Li, J.-M. Hong and X.-Z. You, *J. Mater. Chem.*, 2003, **13**, 1132–1135.
15 W. B. Hu, X. L. Nie and Y. Z. Mi, *Mater. Charact.*, 2010, **61**, 85–89.
16 H.-J. Freund, *J. Am. Chem. Soc.*, 2016, **138**, 8985–8996.
17 J. I. Flege and D. C. Grinter, *Prog. Surf. Sci.*, 2018, **93**, 21–45.
18 M. Monti, B. Santos, A. Mascaraque, O. Rodríguez de la Fuente, M. A. Niño, T. O. Menteş, A. Locatelli, K. F. McCarty, J. F. Marco and J. de la Figuera, *Phys. Rev. B:Condens. Matter Mater. Phys.*, 2012, **85**, 020404.
19 M. Monti, B. Santos, A. Mascaraque, O. Rodríguez de la Fuente, M. A. Nino, T. O. Menteş, A. Locatelli, K. F. McCarty, J. F. Marco and J. de la Figuera, *J. Phys. Chem. C*, 2012, **116**, 11539–11547.
20 L. Martín-García, A. Quesada, C. Munuera, J. F. Fernandez, M. Garca-Hernandez, M. Foerster, L. Aballe and J. de la Figuera, *Adv. Mater.*, 2015, **27**, 5955–5960.
21 A. Mandziak, J. D. L. Figuera, S. Ruiz-Gómez, G. D. Soria, L. Perez, P. Prieto, A. Quesada, M. Foerster and L. Aballe, *Sci. Rep.*, 2018, **8**, 17980.
22 A. Mandziak, J. de la Figuera, A. Quesada, A. Berja, C. Granados-Miralles, J. E. Prieto, L. Aballe, M. Foerster, M. A. Nino and P. Nita, *Ultramicroscopy*, 2023, **253**, 113795.
23 A. Mandziak, G. D. Sori, J. E. Prieto, P. Prieto, C. Granados-Miralles, A. Quesada, M. Foerster, L. Aballe and J. de la Figuera, *Sci. Rep.*, 2019, **9**, 13584.
24 B. Kaemena, S. D. Senanayake, A. Meyer, J. T. Sadowski, J. Falta and J. I. Flege, *J. Phys. Chem. C*, 2013, **117**, 221–232.
25 P. Piercy, *Phys. Rev. B:Condens. Matter Mater. Phys.*, 1992, **45**, 1869–1877.
26 S. Lizzit, A. Baraldi, A. Groso, K. Reuter, M. V. Ganduglia-Pirovano, C. Stampfl, M. Scheffler, M. Stichler, C. Keller, W. Wurth and D. Menzel, *Phys. Rev. B:Condens. Matter Mater. Phys.*, 2001, **63**, 205419.
27 P. K. Wu, M. C. Tringides and M. G. Lagally, *Phys. Rev. B:Condens. Matter Mater. Phys.*, 1989, **39**, 7595–7610.
28 J. I. Flege, J. Hrbek and P. Sutter, *Phys. Rev. B:Condens. Matter Mater. Phys.*, 2008, **78**, 165407.
29 H. Over, *Chem. Rev.*, 2012, **112**, 3356–3426.

30 J. I. Flege, J. Lachnitt, D. Mazur, P. Sutter and J. Falta, *Phys. Chem. Chem. Phys.*, 2015, **18**, 213–219.
31 A. E. Lee, K. E. Singer and D. Tabor, *Proc. R. Soc. London, Ser. A*, 1971, **323**, 523–539.
32 J. C. Batty and R. E. Stickney, *J. Chem. Phys.*, 1969, **51**, 4475–4484.
33 J. C. Batty and R. E. Stickney, *J. Chem. Phys.*, 1969, **51**, 4485–4492.
34 J. C. Batty and R. E. Stickney, *Oxid. Met.*, 1971, **3**, 331–355.
35 I. Langmuir, *J. Am. Chem. Soc.*, 1913, **35**, 105–127.
36 I. Langmuir, *J. Am. Chem. Soc.*, 1915, **37**, 1139–1167.
37 P. J. Feibelman, *Phys. Rev. Lett.*, 2000, **85**, 606–609.
38 W. Ling, N. Bartelt, K. Pohl, J. de la Figuera, R. Hwang and K. McCarty, *Phys. Rev. Lett.*, 2004, **93**, 166101.
39 M. Kalff, G. Comsa and T. Michely, *Phys. Rev. Lett.*, 1998, **81**, 1255–1258.
40 S. Horch, H. Q. Lorensen, S. Helveg, E. Lægsgaard, I. Stensgaard, K. W. Jacobsen, J. K. Norskov and F. Besenbacher, *Nature*, 1999, **398**, 134.
41 T. Skala, N. Tsud, M. N. Orti, T. O. Menteş, A. Locatelli, K. C. Prince and V. Matolin, *Phys. Chem. Chem. Phys.*, 2011, **13**, 7083–7089.
42 T. Skala and V. Matolin, *Surf. Interface Anal.*, 2016, **48**, 111–114.
43 F. V. E. Hensling, W. Braun, D. Y. Kim, L. N. Majer, S. Smink, B. D. Faeth and J. Mannhart, *APL Mater.*, 2024, **12**, 040902.
44 K. Radican, S. I. Bozhko, S.-R. Vadapoo, S. Ulucan, H.-C. Wu, A. McCoy and I. V. Shvets, *Surf. Sci.*, 2010, **604**, 1548–1551.
45 D. Wilgocka-Slezak, T. Giela, K. Freindl, N. Spiridis and J. Korecki, *Appl. Surf. Sci.*, 2020, **528**, 146712.
46 N. Hollmann, Z. Hu, T. Willers, L. Bohaty, P. Becker, A. Tanaka, H. H. Hsieh, H.-J. Lin, C. T. Chen and L. H. Tjeng, *Phys. Rev. B:Condens. Matter Mater. Phys.*, 2010, **82**, 184429.
47 M. W. Haverkort, M. Zwierzycki and O. K. Andersen, *Phys. Rev. B:Condens. Matter Mater. Phys.*, 2012, **85**, 165113.
48 M. Retegan, *Crispy: v0.8.0*, 2024, DOI: **10.5281/zenodo.1008184**.
49 J. Ruiz-Fuertes, S. López-Moreno, J. López-Solano, D. Errandonea, A. Segura, R. Lacomba-Perales, A. Munoz, S. Radescu, P. Rodríguez-Hernandez, M. Gospodinov, L. L. Nagornaya and C. Y. Tu, *Phys. Rev. B:Condens. Matter Mater. Phys.*, 2012, **86**, 125202.
50 F. M. F. de Groot, M. Grioni, J. C. Fuggle, J. Ghijsen, G. A. Sawatzky and H. Petersen, *Phys. Rev. B:Condens. Matter Mater. Phys.*, 1989, **40**, 5715–5723.
51 F. Frati, M. O. J. Y. Hunault and F. M. F. de Groot, *Chem. Rev.*, 2020, **120**, 4056–4110.
52 B. Chen, J. Laverock, L. F. J. Piper, A. R. H. Preston, S. W. Cho, A. DeMasi, K. E. Smith, D. O. Scanlon, G. W. Watson, R. G. Egdell, P.-A. Glans and J.-H. Guo, *J. Phys.: Condens. Matter*, 2013, **25**, 165501.
53 J. F. Moulder, W. F. Stickle, P. E. Sobol and K. D. Bomben, *Handbook of X ray photoelectron spectroscopy: a reference book of standard spectra for identification and interpretation of xps data*, 1995.
54 D. Diaz-Anichtchenko, J. E. Aviles-Coronado, S. López-Moreno, R. Turnbull, F. J. Manjón, C. Popescu and D. Errandonea, *Inorg. Chem.*, 2024, **63**, 6898–6908.
55 W. P. Griffith, *J. Chem. Soc. A*, 1970, 286–291.
56 V. V. Fomichev and O. I. Kondratov, *Spectrochim. Acta, Part A*, 1994, **50**, 1113–1120.
57 J. T. Kloprogge, M. L. Weier, L. V. Duong and R. L. Frost, *Mater. Chem. Phys.*, 2004, **88**, 438–443.
58 R. L. Frost, L. Duong and M. Weier, *Spectrochim. Acta, Part A*, 2004, **60**, 1853–1859.
59 M. N. Iliev, M. M. Gospodinov and A. P. Litvinchuk, *Phys. Rev. B:Condens. Matter Mater. Phys.*, 2009, **80**, 212302.